Review of Scientific Instruments

RESEARCH ARTICLE | JANUARY 24 2024

Development of a large flow electro-hydrostatic actuator equipped with four magnetostrictive-actuated pumps

Mingming Zhang ; Yuchuan Zhu ; Shenghong Ge; Jie Ling

Rev. Sci. Instrum. 95, 015005 (2024)
https://doi.org/10.1063/5.0177567

Review of Scientific Instruments ARTICLE pubs.aip.org/aip/rsi

Development of a large flow electro-hydrostatic actuator equipped with four magnetostrictive-actuated pumps

Cite as: Rev. Sci. Instrum. 95, 015005 (2024); doi: 10.1063/5.0177567
Submitted: 22 September 2023 • Accepted: 30 December 2023 •
Published Online: 24 January 2024

Mingming Zhang,[1] Yuchuan Zhu,[1,a)] Shenghong Ge,[1,2,3] and Jie Ling[1]

AFFILIATIONS

[1] College of Mechanical and Electrical Engineering, Nanjing University of Aeronautics and Astronautics, Nanjing 210016, China
[2] Aviation Key Laboratory of Science and Technology on Aero Electromechanical System Integration, Nanjing Engineering Institute of Aircraft Systems, Nanjing 210061, China
[3] AVIC Nanjing Servo Control System Co, Ltd., Nanjing 210032, China

[a)] **Author to whom correspondence should be addressed:** meeyczhu@nuaa.edu.cn

ABSTRACT

With the advantages of high energy density, high accuracy, and fast response, smart material-driven electro-hydrostatic actuators (SMEHAs) have attracted significant attention in recent years. However, the low flow rate of SMEHAs constrains their application. One potential solution to enhance the flow rate is to increase the number of smart material-actuated pumps. In view of this, this paper proposes a new configuration of an electro-hydrostatic actuator equipped with four magnetostrictive-actuated pumps (FMEHA) to achieve a large flow rate. The mathematical model of the FMEHA is established to investigate the driving phase matching between pumps and the active flow distribution valve. The physical prototype of FMEHA is fabricated. Simulations and experiments are conducted to assess its performance under various driving parameters, including the number of pumps, driving phase, frequency, and amplitude. The optimal driving parameters for the FMEHA are determined based on the results obtained. Experimental findings demonstrate that with a driving phase of 340°, a frequency of 250 Hz, and an amplitude of 20 A, the FMEHA achieves a maximum flow rate of 6.2 l/min.

I. INTRODUCTION

Power-by-wire (PBW) technology, which employs cables rather than hydraulic pipelines for energy transmission, is one of the key technologies for the realization of more electric aircraft and all-electric aircraft.[1,2] Smart material-driven electro-hydrostatic actuators (SMEHAs) are the main actuators of PBW,[3,4] which have the advantages of a simple mechanism,[5] high reliability,[6] high control resolution,[7] and fast response.[8] However, the small stroke of a smart material is only about one-thousandth of its length[9] and results in reduced flow rates, thus impeding the broader application of SMEHAs.[10,11] To improve the flow rate, researchers have proposed different methods.

The maximum flow rate of the available SMEHAs is presented in Fig. 1. It is evident from the figure that most SMEHAs have a flow rate of less than 3 l/min. Larson[12] achieved a large flow by increasing the stroke of smart materials. He designed a SMEHA driven by a 114 mm long, 12 mm diameter Terfenol-D rod with a flow rate of 6 l/min. However, this greatly increases the axial dimensions so that the SMEHA is slender. Chaudhuri *et al.*[13] developed SMEHAs utilizing Terfenol-D rods with lengths of 51 and 102 mm. The corresponding flow rates were 1.488 and 1.362 l/min. They analyzed that the length of the Terfenol-D rod increased, but the generated force decreased at the same diameter. Although the length of the Terfenol-D rod increases, the flow rate of SMEHA decreases. Hence, there are limitations in increasing the length of smart materials to enhance the flow rate of SMEHAs.

Another approach to improve the flow is to increase the number of smart material-driven piston pumps (SMAPs).[14] This method is based on the observation that the flow of SMEHAs scales proportionally with the number of SMAPs. However, due to the increased degree of freedom, the system becomes more complex, and the factors affecting the flow increase. It is necessary to study the driving parameters that impact the output characteristics. Li *et al.*

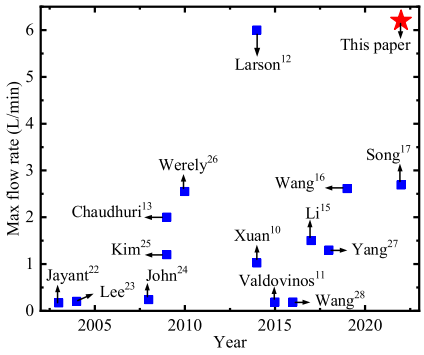

FIG. 1. Summary of the maximum flow rate for electro-hydrostatic actuators driven by smart materials.[10–13,15–17,23–28]

designed an electro-hydrostatic actuation system driven by double kilovolt piezoelectric pumps in parallel.[15] The performance differences under different connection methods and driving methods are studied. The maximum flow rate was 1.5 l/min under the driving frequency of 300 Hz when the asynchronous parallel drive was carried out. Wang *et al.* investigated an active rotary valve integrated into an EHA driven by dual magnetostrictive pumps.[16] The open-loop output flow under different driving current peak-to-peak values and phase angles was tested experimentally. When the driving frequency was 120 Hz, the maximum flow rate was 2.61 l/min. Song *et al.* proposed an axial-mounted dual magnetostrictive pumps-based EHA that used a new type of active rectification valve.[17] The motion of the hydraulic cylinder under different driving signals was analyzed. The experimental results indicated that the maximum flow rate was 2.69 l/min at 180 Hz. These prove that increasing SMAPs can increase the flow rate. The SMEHA can currently integrate two SMAPs, and the flow is still limited.

In order to further improve the flow rate, a new configuration of an electro-hydrostatic actuator equipped with four magnetostrictive-actuated pumps (FMEHA) is proposed. The FMEHA incorporates an active flow distribution valve to rectify the flow generated by its four magnetostrictive-actuated pumps. A mathematical model of FMEHA is established based on the working principle, considering the magnetostrictive hysteresis, the compressibility of the fluid, and the two throttling areas at the active flow distribution valve. The influence of the driving phase matching between the pumps and the active flow distribution valve on the output performance is studied by the established model. Based on this, a series of simulations and experiments are carried out through the model and the fabricated FMEHA prototype. The output characteristics under driving parameters, such as the number of pumps, driving phase, frequency, and amplitude, are investigated. Aiming at the maximum flow rate of FMEHA, the optimal driving parameters are determined.

Compared with the previous work, the novelty of this paper is to realize the integration of four magnetostrictive-actuated pumps to greatly increase the flow rate. The proposed active flow distribution valve can not only rectify the flow of four pumps but also realize the bidirectional movement of FMEHA. In addition, the four magnetostrictive-actuated pumps are driven independently, which can increase the degree of control freedom and allow for more flexible speed regulation.

The rest of this article is organized as follows: Sec. II introduces the structure and working principle of FMEHA. The driving parameters necessary to operate FMEHA are listed. Then, the mathematical model of FMEHA is established in Sec. III. In Sec. IV, the established model is simulated to study the influence of driving phase matching on the output characteristics of FMEHA. Section V presents the experiments and result analysis of the FMEHA's prototype. The optimal driving parameters of FMEHA are obtained. Finally, Sec. VI summarizes this article.

II. STRUCTURE AND WORKING PRINCIPLE OF THE FMEHA

A. Structure of the FMEHA

The structure of the FMEHA, as illustrated in Fig. 2, is mainly composed of magnetostrictive-actuated pumps (MAPs), the active flow distribution valve (AFDV), a servo motor, a manifold, and a hydraulic cylinder. The AFDV comprises a valve spool (AFDVS) and a valve body. The four MAPs are arranged two by two in parallel, making the FMEHA more compact. With the axial arrangement, the number of MAPs can still be increased. The servo motor drives the AFDVS to rotate within the valve body, effectively directing the oil flow through its end faces and sides. Finally, the hydraulic cylinder serves as the actuating component of the FMEHA, connected to the valve body through the manifold.

B. Principle of the FMEHA

As shown in Fig. 3(a), the AFDV connects the MAPs and the hydraulic cylinder. It plays the role of rectification and commutation. There are two throttling areas, as shown in Fig. 3(c). One is axial throttling, and the MAPs are connected to the AFDV through axial throttling holes. The other one is radial throttling, and the hydraulic cylinder is connected to the AFDV through radial throttling holes. The valve body is stationary; however, the AFDVS is rotating all the time, making the two throttling areas change. There are also two types of radial throttling holes, namely long radial throttling holes and short radial throttling holes. The long and short pipes are alternately distributed on the AFDVS's end surface, as shown in Fig. 3(d). The long pipes are marked with blue, and the short pipes are marked

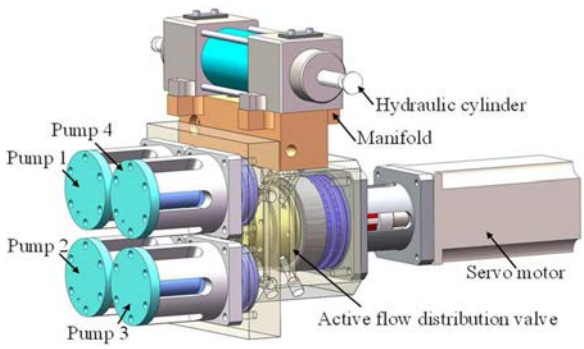

FIG. 2. Structure of the FMEHA.

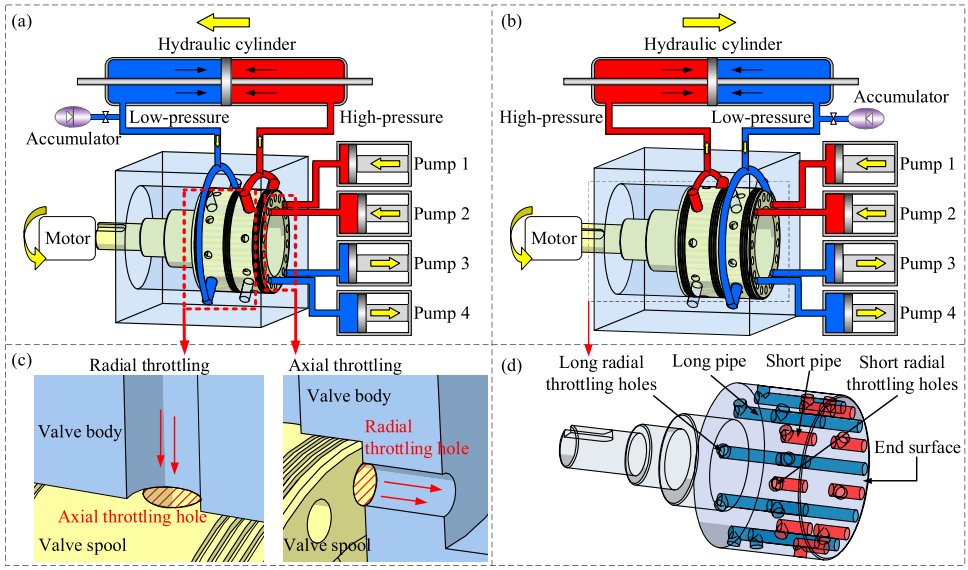

FIG. 3. Working principle of the FMEHA. (a) The working principle of hydraulic cylinder output displacement to the left. (b) The working principle of hydraulic cylinder output displacement to the right. (c) The schematic of the radial throttling and axial throttling. (d) The valve spool of the active flow distribution valve.

with red. When the AFDVS rotates at a uniform speed, the long or short pipes are connected to the outlets of MAPs in turn so that the high- and low-pressure sides are connected to the MAPs in turn to complete the oil rectification. From the difference between Figs. 3(a) and 3(b), it can be seen that when the MAPs discharge oil to the short pipes and absorb oil from the long pipes, the hydraulic cylinder outputs displacement to the left. When the MAPs discharge oil to the long pipes and absorb oil from the short pipes, the hydraulic cylinder outputs displacement to the right. Therefore, changing the driving phase between the MAPs and the AFDV can make the FMEHA output bidirectional movement.

Figure 4(a) shows the matching relationship between the through-flow area and the stroke of the magnetostrictive rod. In one cycle, a MAP is connected to a long pipe and a short pipe once, respectively. Precisely, a MAP is connected to the high-pressure side and the low-pressure side of the hydraulic cylinder once, respectively. One cycle of the MAP can be divided into four stages. At stages I and II, the MAP is connected to the high-pressure side of the hydraulic cylinder, and the through-flow area is positive. Consequently, the length of the magnetostrictive rod extends, facilitating the discharge of oil. Conversely, at stages III and IV, the MAP is connected to the low-pressure side of the hydraulic cylinder, and the through-flow area is negative. This prompts the magnetostrictive rod to contract, allowing for oil absorption. A long pipe and a short pipe are grouped, corresponding to a cycle of MAP. Due to nine groups of pipes, the AFDVS rotates one circle, and the MAPs absorb and discharge oil nine times each. Therefore, the matching relationship between the driving frequency of the MAPs and the rotational speed of the AFDVS is

$$f = N\frac{n}{60}, \tag{1}$$

where f is the frequency of the MAPs' driving current, n is the rotational speed of the AFDVS, and N is the group number of long and short pipes, $N = 9$.

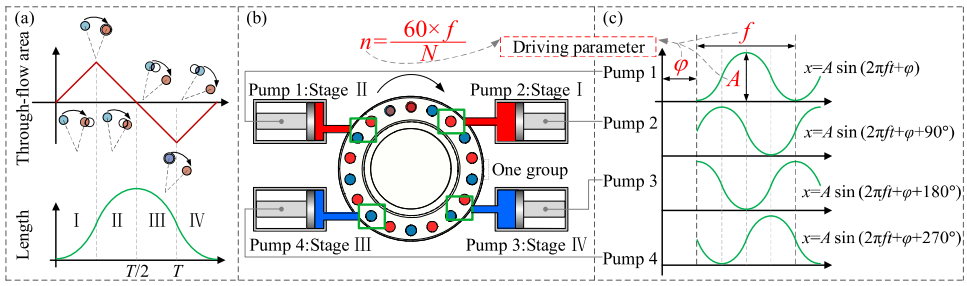

FIG. 4. Driving method of the FMEHA. (a) The matching relationship between the through-flow area and the stroke of the magnetostrictive rod. (b) The position distribution of the four magnetostrictive-actuated pumps. (c) The driving signals of the four magnetostrictive-actuated pumps.

The driving methods of the four MAPs are different. Figure 4(b) shows the position distribution of four MAPs. At the same time, the working states of the four MAPs are different, which are stage II, I, IV, and III, respectively. The driving phase difference among the four MAPs is precisely set at 90°, which correlates with the positional distribution displayed in Fig. 4(c). In addition, the MAPs have a driving phase difference φ from the AFDV to match the motion of AFDV. A change in the driving phase φ by 180° alters the output displacement direction of the FMEHA. By modifying the stroke of the magnetostrictive rod, the driving amplitude profoundly affects the single oil absorption and oil displacement, thereby allowing for adjustments in the flow rate of the FMEHA. Therefore, the driving parameters include the driving phase φ between the MAPs and the AFDV, the driving frequency f of MAPs, the rotation speed n of AFDVS, the driving amplitude A, and the number of MAPs.

III. MATHEMATICAL MODEL OF THE FMEHA

A. Drive voltage–current conversion model

The magnetostrictive rod is magnetized to elongate or shorten within the magnetic field generated by the coil. The coil is driven by a current that is converted by a power amplifier. The power amplifier controls the load current through an internal RC network. Thus, the output current vs the input voltage can be described by the second-order oscillating system,[18]

$$G(s) = \frac{k_U \omega_U^2 (1 + Ts)}{s^2 + 2\xi_U \omega_U s + \omega_U^2}, \tag{2}$$

where k_U is the linear amplification of the power amplifier, T is the time constant of the RC network, and ω_U and ξ_U are the natural frequency and damping ratio, respectively.

B. Magnetization model

The coil is excited by the output current, and the magnetic field is established. Considering the dynamic eddy current effect, the magnetic intensity H can be expressed as[9,19]

$$H = \frac{N_c I}{k_f l_G \left(1 + \mu_0 \mu_G d_G^2 s / 16 k_L \rho_G\right)}, \tag{3}$$

where N_c is the number of coil's turns, I is the input current, k_f is the leakage coefficient, l_G is the length of the magnetostrictive rod, μ_0 is the air permeability, μ_G is the relative permeability of the magnetostrictive rod, d_G is the cross-sectional diameter of the magnetostrictive rod, k_L is the electrical resistivity correction factor, and ρ_G is the resistivity of the magnetostrictive rod.

The magnetization process is described with the Jiles–Atherton (J–A) model,[20]

$$\begin{cases} H_e = H + \alpha M, \\ M = M_r + M_{ir}, \\ M_r = c(M_{an} - M_{ir}), \\ M_{an} = M_s \left[\coth\left(\frac{H_e}{a}\right) - \frac{a}{H_e}\right], \\ M_{ir} = M_{an} - k\delta\left(\frac{dM_{ir}}{dH_e}\right), \end{cases} \tag{4}$$

where H_e is the effective magnetic field intensity, M is the magnetization intensity of the magnetostrictive rod, M_r and M_{ir} are the reversible magnetization and irreversible magnetization, respectively, M_s is the saturation magnetization intensity, α is a mean-field parameter, c is the reversibility coefficient, a is the shape coefficient, k is the pegging coefficient, and $\delta = \mathrm{sign}(dH/dt)$.

C. Magnetostrictive model

Based on the obtained magnetization intensity, the strain of the magnetostrictive rod can be further calculated. It is also related to the saturation magnetostrictive strain and the preload applied to the magnetostrictive rod. The expression for the magnetostrictive strain λ is given by[21]

$$\begin{cases} \lambda = \left(1 + \frac{1}{2}\tanh\frac{2F}{F_s}\right)\lambda_s \frac{M^2}{M_s^2}, & F \le F_s, \\ \lambda = \left(1 - \frac{F - F_s}{F_{max}}\right)\left(1 + \frac{1}{2}\tanh\frac{2F}{F_s}\right)\lambda_s \frac{M^2}{M_s^2}, & F > F_s, \end{cases} \tag{5}$$

where λ_s is the saturation magnetostrictive strain, F_s is the optimum preload, and F_{max} is the maximum magnetostrictive force that can be generated. It can be calculated by

$$F_{max} = \frac{3}{2}\lambda_s E_G A_G, \tag{6}$$

where E_G and A_G are Young's modulus and the cross-sectional area of the magnetostrictive rod, respectively.

Based on the magnetostrictive strain, the output magnetostrictive force F_G can be further calculated as

$$F_G = \lambda E_G A_G. \tag{7}$$

D. Mechanical dynamic model

The structure schematic of the MAP is shown in Fig. 5. As each part affects the output displacement of the plunger, the dynamic models for the magnetostrictive rod, output rod, and plunger are developed separately,

$$\begin{cases} m_G \ddot{x}_G = F_G - k_G x_G - c_G \dot{x}_G - k_o(x_G - x_o) - c_o(\dot{x}_G - \dot{x}_o), \\ m_o \ddot{x}_o = k_o(x_G - x_o) + c_o(\dot{x}_G - \dot{x}_o) - k_b x_o - c_b \dot{x}_o - k_p(x_o - x_p) - c_p(\dot{x}_o - \dot{x}_p), \\ m_p \ddot{x}_p = k_p(x_o - x_p) + c_p(\dot{x}_o - \dot{x}_p) - p_{ch} A_p, \end{cases} \tag{8}$$

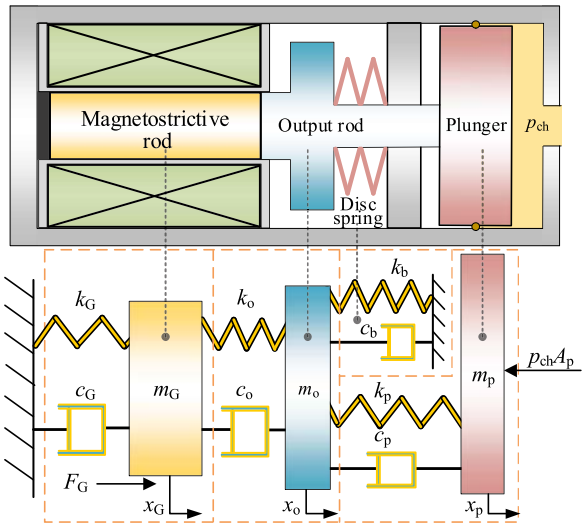

FIG. 5. Schematic of the magnetostrictive-actuated pump's structure.

where m_G, m_o, and m_p are the masses of the magnetostrictive rod, output rod, and plunger, respectively; c_G, c_o, c_b, and c_p are the damping of the magnetostrictive rod, output rod, disk spring, and plunger, respectively; k_G, k_o, k_b, and k_p are the stiffness of the magnetostrictive rod, output rod, disk spring, and plunger, respectively; x_G, x_o, and x_p are the displacements of the magnetostrictive rod, output rod, and plunger, respectively; A_p is the area of the plunger; and p_{ch} is the pressure of the pump chamber.

E. Hydrodynamic model of the pump cavity

The mechanical–hydraulic energy conversion occurs in the pump chamber. When the magnetostrictive rod is elongated, the oil in the pump chamber is compressed, and the pressure rises. According to the fluid continuity equation,[22] the pump chamber pressure is shown as

$$\dot{p}_{ch} = \beta_e \frac{A_p \dot{x}_p + Q_{in} - Q_{out}}{A_p (h_p - x_p)}, \tag{9}$$

where Q_{in} and Q_{out} are the inlet and outlet flows of the pump chamber, respectively, h_p is the initial height of the pump cavity, and β_e is the effective bulk modulus of the oil. The oil is mixed with air and exists in the form of air bubbles. This leads to a reduction in the bulk modulus of the oil,

$$\frac{1}{\beta_e} = \frac{\delta_a p_a}{p_{ch}^2} + \left(1 - \frac{\delta_a p_a}{p_{ch}}\right)\frac{1}{\beta_f}, \tag{10}$$

where β_f is the bulk modulus of the pure oil, p_a is the atmospheric pressure, and δ_a is the volume fraction of oil mixed with gas at atmospheric pressure.

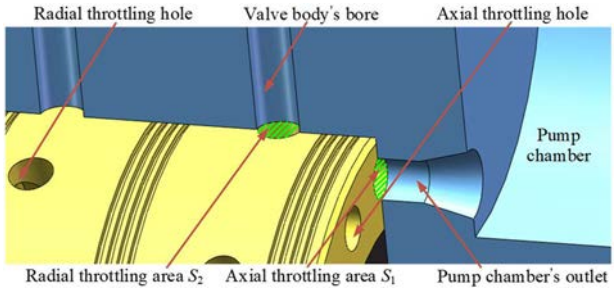

FIG. 6. Schematic of the active flow distribution valve's through-flow area.

F. Throttling model of the active flow distribution valve

As shown in Fig. 6, the oil is throttled twice at the AFDV. Therefore, the equivalent through-flow area S of the AFDV consists of the axial throttling area S_1 and the radial throttling area S_2. The equivalent through-flow area is obtained from the series effect,

$$\frac{1}{S^2} = \frac{1}{S_1^2} + \frac{1}{S_2^2}. \tag{11}$$

In addition, the variation pattern of S_1 and S_2 in a cycle is shown in Fig. 7. Due to the large curvature, the cylindrical surface can be extended as a plane. The rotation angle of the radial throttling hole is represented by the distance x,

$$x = \frac{\theta}{4\theta_0}\frac{2\pi R_2}{9}, \tag{12}$$

where θ_0 is the central angle corresponding to the tangency of the pump chamber's outlet and axial throttling hole and R_2 is the radius of the AFDVS.

d_a is the center distance between the pump chamber's outlet and the axial throttling hole,

$$d_a = \begin{cases} 2R_1 \sin\left(|\theta_0/2 - \theta/2|\right), & 0 \le \theta < 2\theta_0, \\ 2R_1 \sin\left(|\theta_0/2 - (\theta - 2\theta_0)/2|\right), & 2\theta_0 \le \theta < 4\theta_0, \end{cases} \tag{13}$$

where R_1 is the distribution radius of the pipes.

It can be seen from the figure that the axial throttling area S_1 first becomes larger and then smaller. While the radial throttling area S_2 undergoes an initial enlargement, remains constant in the middle, and finally diminishes. This behavior is attributed to the valve body's larger bore diameter in comparison with the radial throttling hole. Therefore, the equations for S_1 and S_2 in one cycle can be derived as follows:

$$S_1 = \begin{cases} 2{r_1}^2 \arccos\dfrac{d_a}{2r_1} - r_1 d_a \sin\left(\arccos\dfrac{d_a}{2r_1}\right), & 0 \le \theta < 2\theta_0, \\ -2{r_1}^2 \arccos\dfrac{d_a}{2r_1} + r_1 d_a \sin\left(\arccos\dfrac{d_a}{2r_1}\right), & 2\theta_0 \le \theta < 4\theta_0, \end{cases} \tag{14}$$

$$S_2 = \begin{cases} r_1^2 \arccos\dfrac{r_1^2 + d_r^2 - r_2^2}{2r_1 d_r} + r_2^2 \arccos\dfrac{r_2^2 + d_r^2 - r_1^2}{2r_2 d_r}, & 0 < x < x_1, \\ -r_1 d_r \sin\left(\arccos\dfrac{r_1^2 + d_r^2 - r_2^2}{2r_1 d_r}\right), & \text{or } x_2 < x < x_1 + x_2, \\ 2\pi r_1^2, & x_1 < x < x_2 \\ -r_1^2 \arccos\dfrac{r_1^2 + d_r^2 - r_2^2}{2r_1 d_r} - r_2^2 \arccos\dfrac{r_2^2 + d_r^2 - r_1^2}{2r_2 d_r}, & x_1 + x_2 < x < 2x_1 + x_2, \\ +r_1 d_r \sin\left(\arccos\dfrac{r_1^2 + d_r^2 - r_2^2}{2r_1 d_r}\right), & \text{or } x_1 + 2x_2 < x < 2x_1 + 2x_2, \\ -2\pi r_1^2, & 2x_1 + x_2 < x < x_1 + 2x_2, \end{cases} \tag{15}$$

where r_1 is the radius of the pump chamber's outlet and the axial and radial throttling holes and r_2 is the radius of the valve body's bore. The equivalent center distance d_r between the radial throttling hole and the valve body's bore is calculated as

$$d_r = \begin{cases} |(x_1 + x_2)/2 - x|, & 0 \le x < x_1 + x_2, \\ |(x_1 + x_2)/2 - (x - x_1 - x_2)|, & x_1 + x_2 \le x < 2x_1 + 2x_2, \end{cases} \tag{16}$$

where x_1 and x_2 can be expressed as

$$x_1 = 2R_2 \arcsin\left(\frac{r_1}{R_2}\right), \tag{17}$$

$$x_2 = 2R_2 \arcsin\left(\frac{r_2}{R_2}\right). \tag{18}$$

The flow rates Q_{out} and Q_{in} can be obtained as

$$Q_{out} = \text{sign}\,(p_{ch} - p_{th}) C_d |S| \sqrt{\frac{2}{\rho}|p_{ch} - p_{th}|}, \quad S > 0, \tag{19}$$

$$Q_{in} = \text{sign}\,(p_{tl} - p_{ch}) C_d |S| \sqrt{\frac{2}{\rho}|p_{tl} - p_{ch}|}, \quad S < 0, \tag{20}$$

where p_{th} and p_{tl} are the pressures of the high- and low-pressure sides, respectively, ρ is the oil density, and C_d is the flow coefficient, according to the practical value of 0.65–0.7.

G. The model of pressure drop in hydraulic pipes

The pressure drop of oil through the pipe mainly includes the local loss and the pressure drop caused by the fluid inductance and the fluid resistance. Considering the actual flow state of the oil, the pressure drop is modeled under laminar flow. Then, the calculation is as follows:

$$p_{th} - p_h = L_{th}\dot{Q}_{out} + R_{th}Q_{out} + \Delta p_\zeta, \tag{21}$$

$$p_l - p_{tl} = L_{tl}\dot{Q}_{in} + R_{tl}Q_{in} + \Delta p_\zeta, \tag{22}$$

where p_h and p_l are the pressures of the two chambers, respectively; L_{th} and L_{tl} are the fluid inductances of the high- and low-pressure pipes, respectively; R_{th} and R_{tl} are the fluid resistances of the high- and low-pressure pipes, respectively; and Δp_ζ is the sum of the local loss.

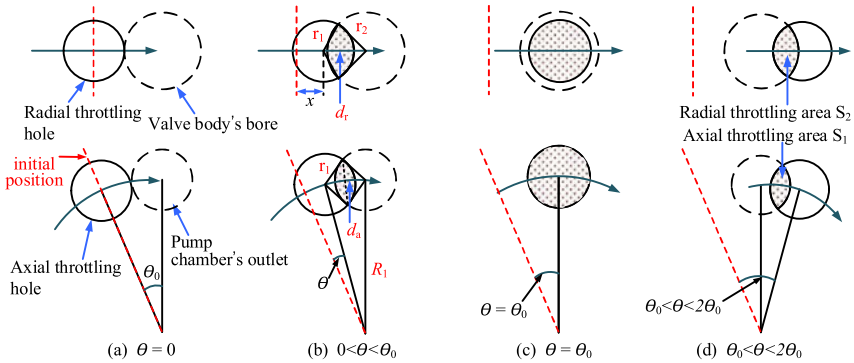

FIG. 7. Variation process of the through-flow area.

H. The dynamic model of the hydraulic cylinder

As the final actuator of FMEHA, the hydraulic cylinder's piston rod overcomes the frictional and load resistances to output displacement by utilizing the differential pressure existing between the two chambers. The dynamic differential equation for this behavior is expressed as follows:

$$(m_r + m_L)\ddot{x}_r + c_r\dot{x}_r = (p_h - p_l)A_r - F_f - F_L, \tag{23}$$

where m_r and m_L are the masses of the piston rod and the load, respectively; c_r, x_r, and A_r are the damping, displacement, and action area of the piston rod, respectively; F_f is the frictional force between the piston and the inner wall of the cylinder; and F_L is the externally applied load force.

IV. SIMULATION MODEL AND ANALYSIS OF THE FMEHA

The simulation model of the FMEHA is built in MATLAB/Simulink, as shown in Fig. 8. Table I shows some simulation parameters. By utilizing this simulation model, it becomes conveniently possible to evaluate the effect of each driving parameter on the output performance.

A. The driving phase matching between MAPs and AFDV

There is an important matching in the FMEHA: the driving phase matching between the MAPs and the AFDV. The optimal driving phase matching is that when the MAP is connected to the high-pressure side of the hydraulic cylinder, the MAP discharges the oil. When the MAP is connected to the low-pressure side, the MAP absorbs oil. In the incomplete driving phase matching, the MAP may absorb oil from the high-pressure side or discharge oil to the low-pressure side. This incomplete matching reduces the rectification efficiency and the output flow of the FMEHA. This section

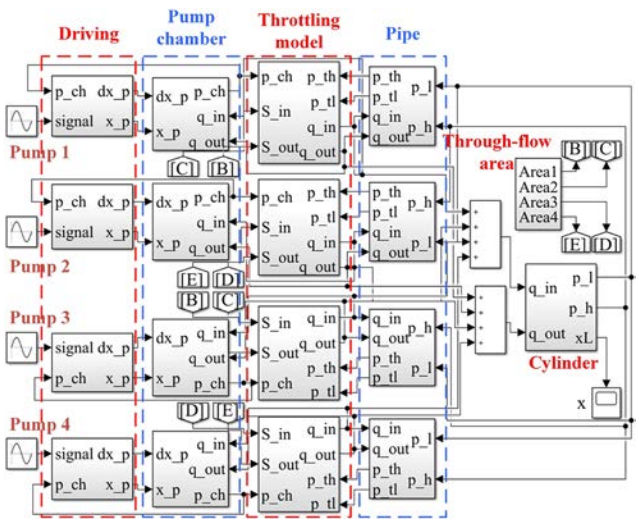

FIG. 8. Simulation model of the FMEHA.

TABLE I. Parameters of the FMEHA model.

Name	Unit	Value	Name	Unit	Value	Name	Unit	Value
N_c	⋯	500	k_f	⋯	1.1	a	kA/m	7.012
α	⋯	−0.02	c	⋯	0.18	k	⋯	4.283
M_s	kA/m	600	λ_s	ppm	1100	μ_0	H/m	$4\pi \times 10^{-7}$
μ_G	⋯	9	l_G	m	0.04	d_G	m	0.013
ρ_G	Ω m	6×10^{-7}	E_G	GPa	30	m_G	kg	0.06
c_G	N s/m	1280	m_o	kg	0.021	m_p	kg	0.042
k_d	N/m	3.24×10^6	c_d	N·s/m	2500	A_p	m^2	1.73×10^{-3}
h_p	m	0.005	β_f	MPa	1800	ρ	kg/m^3	850
δ_a	⋯	0.05	r_1	m	0.002	r_2	m	0.0026
R_1	m	0.023	R_2	m	0.027	A_r	m^2	6.3×10^{-4}

discusses the optimal driving phase matching, under-matching, and over-matching between the MAPs and the AFDV.

Figure 9(a) shows the optimal driving phase matching at 200 Hz. The black curve represents the output displacement of the magnetostrictive rod, and the red curve represents the output velocity of the rod v. The green curve represents the through-flow area S. When the through-flow area is positive, it means that the MAP is connected to the high-pressure side of the hydraulic cylinder. When the through-flow area is negative, it means that the MAP is connected to the low-pressure side. It can be seen from the figure that when the magnetostrictive rod elongates, the through-flow area is positive. The MAP discharges oil to the high-pressure side. Both the velocity and the through-flow area are positive. When the magnetostrictive rod is shortened, the area is negative. The MAP absorbs oil to the low-pressure side. Both the velocity and the flow area are negative. At the optimal driving phase matching, the rectification flow rate Q_{rec_op} in one period T can be expressed as

$$Q_{rec\_op} = \int_0^T Q_{op\_t}\,\mathrm{d}t = \int_0^T |v \cdot S|\,\mathrm{d}t, \tag{24}$$

where Q_{op_t} is the rectification flow between the MAPs and the AFDV at each moment, when the matching is optimal. The velocity v and the through-flow area S have the same sign, resulting in a positive value for Q_{op_t}. Under this driving phase matching, there is no rectification loss in the FMEHA.

Figures 9(b) and 9(c) show the under-matching and over-matching, respectively. When the area is positive, both of them have the shortening of the magnetostrictive rod, which causes the MAP to absorb oil from the high-pressure side. There is a situation where the velocity v is negative. When the area is negative, both of them have the elongation of the magnetostrictive rod, which causes the MAP to discharge oil to the low-pressure side. There is a situation where the velocity v is positive. The rectification flow Q_{rec_un} at under-matching and Q_{rec_ov} at over-matching can be expressed as

$$Q_{rec\_un} = \int_0^T Q_{un\_t}\,\mathrm{d}t = -\int_0^{t_o} |v \cdot S|\,\mathrm{d}t + \int_{t_o}^{\frac{T}{2}} |v \cdot S|\,\mathrm{d}t - \int_{\frac{T}{2}}^{\frac{T}{2}+t_o} |v \cdot S|\,\mathrm{d}t + \int_{\frac{T}{2}+t_o}^{T} |v \cdot S|\,\mathrm{d}t, \tag{25}$$

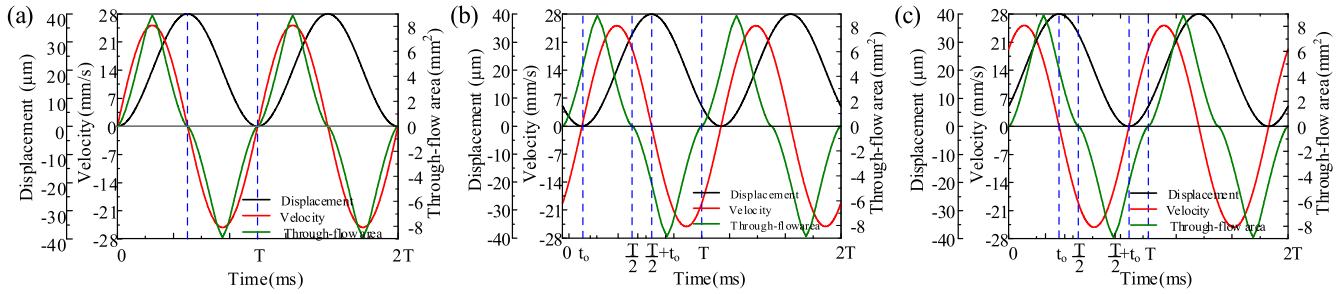

FIG. 9. Driving phase matching between the magnetostrictive-actuated pumps and the active flow distribution valve. (a) Optimal driving phase matching. (b) Under-matching. (c) Over-matching.

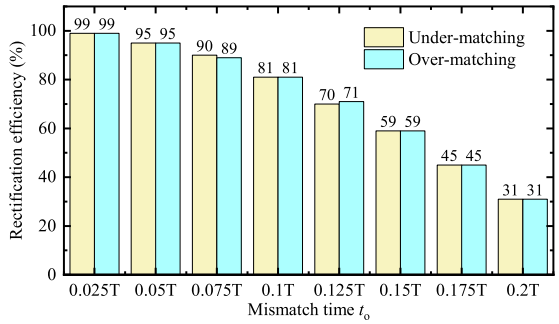

FIG. 10. Rectification efficiency of under-matching and over-matching at different mismatch times.

$$Q_{rec\_ov} = \int_0^T Q_{ov\_t}\,dt = \int_0^{t_o} |v \cdot S|\,dt - \int_{t_o}^{\frac{T}{2}} |v \cdot S|\,dt + \int_{\frac{T}{2}}^{\frac{T}{2}+t_o} |v \cdot S|\,dt - \int_{\frac{T}{2}+t_o}^{T} |v \cdot S|\,dt, \quad (26)$$

where Q_{un_t} and Q_{ov_t} are the rectification flows at each moment of under-matching and over-matching, respectively, t_o represents the mismatch time between the MAPs and the AFDV, which can be calculated by driving the frequency and phase. According to formulas (24)–(26), the rectification flow of under-matching and over-matching is less than that of optimal driving phase matching due to the different signs of velocity v and through-flow area S. The following is a discussion of rectification efficiency without considering the change of output pressure. Based on formulas (24)–(26), the rectification efficiency of under-matching and over-matching at different mismatch times t_o is illustrated in Fig. 10. Here, t_o is relative to a period T. It can be observed that the rectification efficiency decreases at an accelerating rate as the mismatch time t_o increases. By controlling the mismatch time within 0.05 T, the decrease in rectification efficiency can be ensured to remain below 5%. When the mismatch time t_o is 0.2 T, the rectification efficiency drops to 31%. The under-matching and over-matching are similar in the decrease with the mismatching time t_o.

Furthermore, when the absolute value of the through-flow area reaches the maximum, the magnetostrictive rod is growing or decelerating. The velocity of the magnetostrictive rod does not reach the maximum at this time, which will affect the rectification, thereby reducing the output flow of the FMEHA.

Therefore, the driving phase matching between the MAPs and the AFDV regulates the flow rate by affecting the rectification efficiency. Section IV B discusses the effect of driving phase matching on the flow rate of FMEHA.

B. Simulation analysis of driving frequency and phase on flow rate

The driving phase matching between the MAPs and the AFDV is adjusted by the driving phase of MAPs. Figure 11 shows the flow rates of single, double, triple, and quadruple MAPs at different driving frequencies and phases. The negative flow indicates the reverse

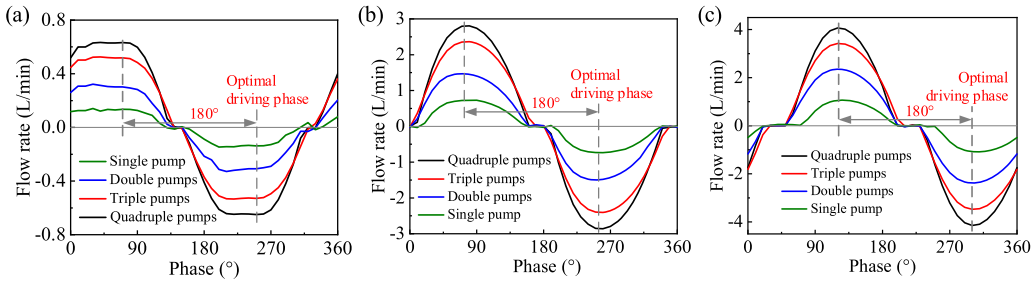

FIG. 11. Flow rate at different driving frequencies and phases: (a) 50 Hz, (b) 150 Hz, and (c) 250 Hz.

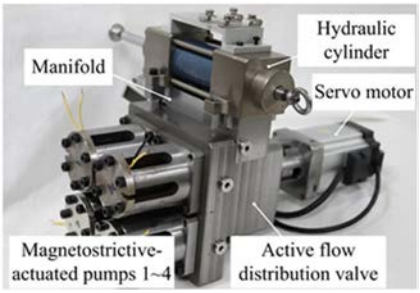

FIG. 12. Prototype of the FMEHA.

output displacement. It is evident that the flow rate follows a sinusoidal pattern as the driving phase varies. With an increasing driving frequency, the optimal driving phase gradually rises. This is because the rise in driving frequency exacerbates the magnetization hysteresis. Simultaneously, the shortened individual cycle, coupled with the inertia of the oil, makes it more challenging for the oil to be discharged or absorbed by the MAPs in time. Consequently, the driving signal needs to be advanced further. Moreover, the driving phase enables a bidirectional motion in the FMEHA. When the output flow is equal, the driving phase difference between the forward and reverse motions is 180°.

In addition, it is worth noting that the optimal driving phase remains relatively consistent across different numbers of MAPs, given the same driving frequency. It indicates that each MAP is matched independently and similarly to the AFDV. The quantity of MAPs does not affect the optimal driving phase. It can also be observed that each MAP can work independently, which is decoupled.

V. EXPERIMENTAL INVESTIGATION OF THE FMEHA

The prototype of FMEHA is fabricated, as shown in Fig. 12. A series of experiments are carried out to verify the accuracy of the simulation model and evaluate the effect of each driving parameter on the output performance of FMEHA.

The test platform of FMEHA is built, and its schematic and physical diagrams are shown in Fig. 13. The flow rate of the FMEHA is calculated indirectly by the output velocity of the hydraulic cylinder's piston rod, which is measured by the laser displacement sensor (CD-33, Sixin).

The servo motor (Panasonic MSMF042L1U2M) drives the AFDVS to rotate at a uniform speed. The servo driver (A6 MBDLT25SF) is supplied with stable two-phase pulses by the computer and the motor controller (Leadshine SMC304). The DSP controller (TMS320F28335) receives the information from the motor encoder and calculates the driving signal of MAPs in real time to ensure that the MAPs maintain a fixed driving matching with the AFDV. The four MAPs operate at the same driving amplitude and frequency, with each driving phase lagged by 90°. The power amplifiers (AE Techron, 7224) convert the driving signals into current signals.

A. Phase–flow characteristics

Figures 14(a)–14(c) show the flow rate of FMEHA with the driving phase when the driving frequency is 50, 150, and 250 Hz, respectively. The driving amplitude is 8 A. These figures indicate that the simulation model effectively predicts the changes in flow corresponding to the driving phase at various frequencies. The flow rate exhibits a sinusoidal variation in relation to the driving phase. Specifically, at 50, 150, and 250 Hz, the optimal driving phases are observed to be 200°, 260°, and 340°, respectively. Notably, as the driving frequency increases, the optimal driving phase also increases, in line with the previously discussed reasons. Importantly, a change in the driving phase of 180° leads to a corresponding reversal in the flow rate, confirming the ability of the driving phase to adjust the flow rate and introduce a bidirectional motion in the FMEHA.

B. Frequency–flow characteristics

Based on the feature that each MAP can work independently, experiments with double, triple, and quadruple MAPs are carried

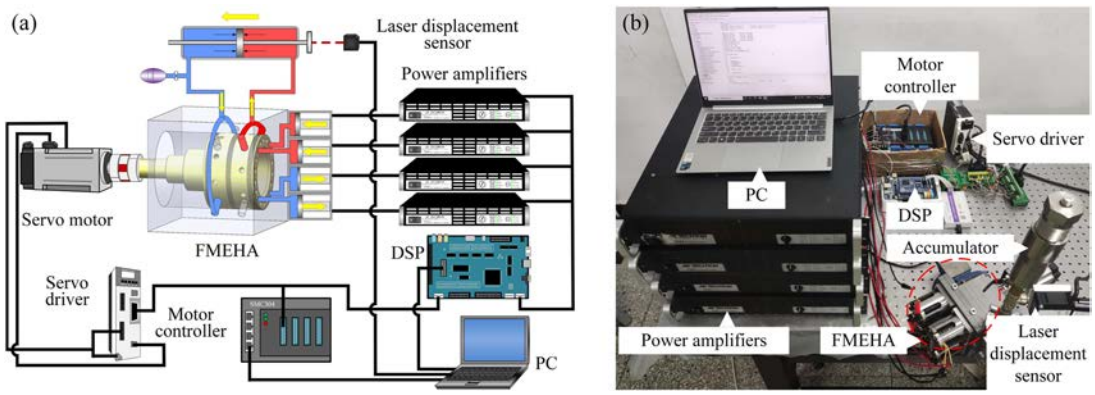

FIG. 13. Test platform of the FMEHA: (a) schematic diagram and (b) physical diagram.

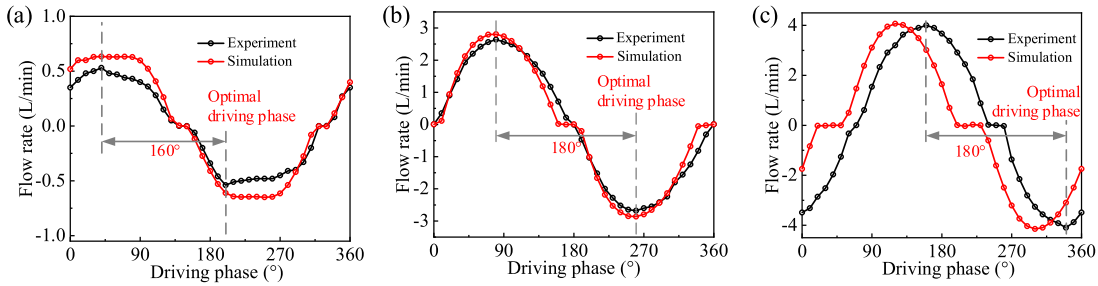

FIG. 14. Flow with different phases under different driving frequencies: (a) 50 Hz, (b) 150 Hz, and (c) 250 Hz.

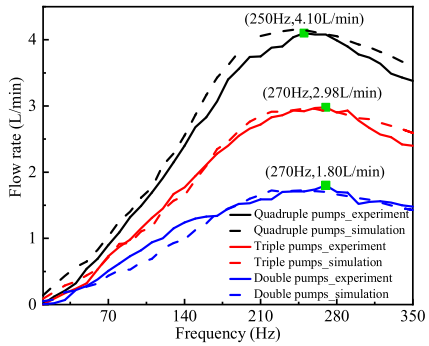

FIG. 15. Flow rate of the FMEHA at different driving frequencies under different pumps.

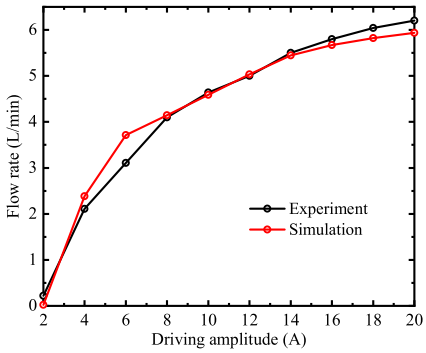

FIG. 16. Flow rate of the FMEHA under different driving amplitudes.

out. Figure 15 presents the maximum flow rate (at the optimal driving phase) corresponding to each driving frequency in the simulation and experiment. The driving amplitude is 8 A. This figure demonstrates that the simulation model can accurately predict the variation trend of FMEHA with frequency under different numbers of MAPs. The maximum flow rate of FMEHA is measured to be 1.8, 2.98, and 4.1 l/min for double, triple, and quadruple MAPs, respectively. The optimal driving frequencies are 270, 270, and 250 Hz, respectively. Notably, the optimal driving frequency exhibits small fluctuations for different MAPs' configurations. Thus, it can be inferred that the number of MAPs has little effect on the optimal driving frequency. Furthermore, the reason why the flow rate increases first and then decreases is that a higher frequency means more times of oil suction and discharge. However, at higher frequencies, the magnetostrictive rod's stroke will be attenuated. Moreover, due to inertia, oil is not easily sucked in or discharged at high frequencies.

C. Amplitude–flow characteristics

The flow rate with the driving amplitude is shown in Fig. 16, where the flow rate is obtained at the optimal driving frequency and phase. The flow rate is positively correlated with the driving amplitude. When the driving amplitude is 20 A, the FMEHA reaches a maximum flow rate of 6.2 l/min. The coil turns are 500, and the magnetization intensity is 250 000 A/m. This figure illustrates a significant increase in the flow rate as the driving amplitude is raised, particularly at lower driving amplitudes. However, once the amplitude exceeds 8 A, the rate of flow rate increase diminishes due to the approaching saturation of the magnetostrictive rod's stroke.

VI. CONCLUSION

In this article, a novel configuration of an electro-hydrostatic actuator equipped with four magnetostrictive-actuated pumps (FMEHA) is proposed to improve the flow rate. The simulations and experiments are carried out. In addition, the output characteristics of FMEHA under driving parameters are studied. The conclusions can be made as follows:

(1) The electro-hydrostatic actuator with four magnetostrictive-actuated pumps, rectified by the active flow distribution valve, has demonstrated notable advancements in the flow rate. This presents an alternative framework for large-flow SMEHAs.
(2) The established mathematical model is in good agreement with the experimental results. The model can describe the behavior of FMEHA under different working conditions, which provides an effective research method for the following work.

(3) There is an optimal driving phase matching between the pumps and the active flow distribution valve. The driving phase can regulate the flow, but this is at the expense of rectification efficiency. Altering the driving phase by 180° results in reverse motion output by the FMEHA.
(4) The optimal driving frequency is independent of the number of pumps. The flow rate is positively correlated with the driving amplitude. The suggested optimal driving parameters for FMEHA are a driving phase of 340°, a driving frequency of 250 Hz, and a driving amplitude of 20 A. Under these conditions, the FMEHA achieves a maximum flow rate of 6.2 l/min.

Future research, based on this study, will concentrate on optimizing the magnetic circuit to maximize the stroke of the magnetostrictive rod and the flow channel structure to minimize the pressure drop. These approaches are expected to further increase the flow rate of FMEHA while facilitating volume reduction.

ACKNOWLEDGMENTS

This work was supported by the National Natural Science Foundation of China (Grant No. 51975275) and the Primary Research and Development Plan of Jiangsu Province (Grant No. BE2021034).

AUTHOR DECLARATIONS

Conflict of Interest

The authors have no conflicts to disclose.

Author Contributions

Mingming Zhang: Conceptualization (equal); Data curation (equal); Formal analysis (equal); Investigation (equal); Methodology (equal); Software (equal); Validation (equal); Visualization (equal); Writing – original draft (equal); Writing – review & editing (equal). **Yuchuan Zhu**: Conceptualization (equal); Formal analysis (equal); Funding acquisition (equal); Methodology (equal); Project administration (equal); Supervision (equal); Writing – review & editing (equal). **Shenghong Ge**: Formal analysis (equal); Project administration (equal); Supervision (equal); Validation (equal); Writing – review & editing (equal). **Jie Ling**: Investigation (equal); Methodology (equal); Supervision (equal); Validation (equal); Writing – review & editing (equal).

DATA AVAILABILITY

The data that support the findings of this study are available from the corresponding author upon reasonable request.

REFERENCES

[1] J. Chen, X. Zhang, and C. Wen, "Harmonics attenuation and power factor correction of a more electric aircraft power grid using active power filter," IEEE Trans. Ind. Electron. **63**, 7310–7319 (2016).
[2] M. Borghei and M. Ghassemi, "Insulation materials and systems for more- and all-electric aircraft: A review identifying challenges and future research needs," IEEE Trans. Transp. Electrif. **7**, 1930–1953 (2021).
[3] A. Navatha, K. Bellad, S. S. Hiremath, and S. Karunanidhi, "Dynamic analysis of electro hydrostatic actuation system," Procedia Technol. **25**, 1289–1296 (2016).
[4] R. Wang, Y. Zhu, Y. Jiang, and L. Chen, "Research on position control of bidirectional dual magnetostrictive rods-based electro-hydrostatic actuator with active rotary valve," Smart Mater. Struct. **29**, 035003 (2020).
[5] C. Zhang, C. Zhu, B. Meng, and S. Li, "Challenges and solutions for high-speed aviation piston pumps: A review," Aerospace **8**, 392 (2021).
[6] C.-h. Lin and Y.-Z. Lin, "Analysis of nonlinear piezomagnetism for magnetostrictive Terfenol-D composites," J. Magn. Magn. Mater. **540**, 168490 (2021).
[7] L. Chen, Y. Zhu, J. Ling, and M. Zhang, "Temperature dependence modeling and experimental evaluation of a multidimensional discrete magnetostrictive actuator," Appl. Therm. Eng. **230**, 120736 (2023).
[8] J. Zhou, Z. He, C. Rong, and G. Xue, "A giant magnetostrictive rotary actuator: Design, analysis and experimentation," Sens. Actuators, A **287**, 150–157 (2019).
[9] L. Chen, Y. Zhu, J. Ling, and Z. Feng, "Theoretical modeling and experimental evaluation of a magnetostrictive actuator with radial-nested stacked configuration," Nonlinear Dyn. **109**, 1277–1293 (2022).
[10] Z. Xuan, T. Jin, N. S. Ha, N. S. Goo, T. H. Kim, B. W. Bae, H. S. Ko, and K. W. Yoon, "Performance of piezo-stacks for a piezoelectric hybrid actuator by experiments," J. Intell. Mater. Syst. Struct. **25**, 2212–2220 (2014).
[11] J. Valdovinos and G. P. Carman, "Development of a low-voltage piezohydraulic pump for compact hydraulic systems," Smart Mater. Struct. **24**, 125008 (2015).
[12] J. P. Larson, "Design of a magnetostrictive-hydraulic actuator considering nonlinear system dynamics and fluid-structure coupling," Ph.D. thesis, The Ohio State University, 2014.
[13] A. Chaudhuri, J.-H. Yoo, and N. M. Wereley, "Design, test and model of a hybrid magnetostrictive hydraulic actuator," Smart Mater. Struct. **18**, 085019 (2009).
[14] S. L. Herdic, "Development of piezo-hydraulic actuation systems technology for use on a helicopter trailing edge flap," Ph.D. thesis, Georgia Institute of Technology, 2005.
[15] Y. Li, V. T. Le, N. S. Goo, T. H. Kim, and C. S. Lee, "High actuation force of piezoelectric hybrid actuator with multiple piezoelectric pump design," J. Intell. Mater. Syst. Struct. **28**, 2557–2571 (2017).
[16] Z. Wang, Y. Zhu, R. Li, C. Liu, and N. Bruno, "Development of a dual magnetostrictive material rods–based electro-hydrostatic actuator," J. Intell. Mater. Syst. Struct. **30**, 1871–1881 (2019).
[17] Y. Zhu, C. Liu, Y. Song, L. Chen, Y. Jiang, and C. Wu, "Research on an axial-mounted dual magnetostrictive material rods-based electro-hydrostatic actuator," J. Intell. Mater. Syst. Struct. **33**, 330–341 (2022).
[18] Y. Zhu, X. Yang, and N. M. Wereley, "Research on hysteresis loop considering the prestress effect and electrical input dynamics for a giant magnetostrictive actuator," Smart Mater. Struct. **25**, 085030 (2016).
[19] Y. Zhu, X. Yang, and N. M. Wereley, "Theoretical and experimental investigations of a magnetostrictive electro-hydrostatic actuator," Smart Mater. Struct. **27**, 105043 (2018).
[20] D. C. Jiles, J. Thoelke, and M. Devine, "Numerical determination of hysteresis parameters for the modeling of magnetic properties using the theory of ferromagnetic hysteresis," IEEE Trans. Magn. **28**, 27–35 (1992).
[21] L. Sun and X. Zheng, "Numerical simulation on coupling behavior of Terfenol-D rods," Int. J. Solids Struct. **43**, 1613–1623 (2006).
[22] J. Sirohi and I. Chopra, "Design and development of a high pumping frequency piezoelectric-hydraulic hybrid actuator," J. Intell. Mater. Syst. Struct. **14**, 135–147 (2003).
[23] D. G. Lee, S. W. Or, and G. P. Carman, "Design of a piezoelectric-hydraulic pump with active valves," J. Intell. Mater. Syst. Struct. **15**, 107–115 (2004).
[24] S. John, A. Chaudhuri, and N. M. Wereley, "A magnetorheological actuation system: Test and model," Smart Mater. Struct. **17**, 025023 (2008).

[25]G. W. Kim, "Design and nonlinear force control of a power-by-wire piezoelectric-hydraulic pump actuator for automotive transmissions," Ph.D. thesis, The Pennsylvania State University, 2009.
[26]A. Chaudhuri and N. M. Wereley, "Experimental validation of a hybrid electrostrictive hydraulic actuator analysis," J. Vib. Acoust. **132**, 021006 (2010).
[27]X. Yang, Y. Zhu, and Y. Zhu, "Characteristic investigations on magnetic field and fluid field of a giant magnetostrictive material-based electro-hydrostatic actuator," Proc. Inst. Mech. Eng., Part G **232**, 847–860 (2018).
[28]L. Wang, "Design of a variable trailing edge camber wing based on the piezoelectric hydraulic pump," Master's thesis, Harbin Institute of Technology, 2016.